# Polarity-Driven Polytypic Branching in Cu-Based Quaternary Chalcogenide Nanostructures

Reza R. Zamani,[*,†,‡] Maria Ibáñez,[‡] Martina Luysberg,[¶] Nuria García-Castelló,[§] Lothar Houben,[¶] Joan Daniel Prades,[§] Vincenzo Grillo,[∥,⊥] Rafal E. Dunin-Borkowski,[¶] Joan Ramón Morante,[‡,§] Andreu Cabot,[‡,#] and Jordi Arbiol[*,†,#]

*Institut de Ciència de Materials de Barcelona (ICMAB-CSIC), Campus de la UAB, Bellaterra 08193, Spain, Catalonia Institute for Energy Research (IREC), Jardins de les Dones de Negre 1, Sant Adrià del Besòs, Barcelona 08930, Spain, Ernst Ruska-Centre for Microscopy and Spectroscopy with Electrons, Forschungszentrum Jülich GmbH, Jülich 52425, Germany, Departament d'Electrònica, Universitat de Barcelona, Barcelona 08028, Spain, Centro S3,CNR–Istituto di Nanoscienze, Via Campi 213A, Modena 41125,Italy, IMEM–CNR, Parco Area delle Scienze 37/A, Parma 43010,Italy, and Institució Catalana de Recerca i Estudis Avançats (ICREA), Barcelona 08010, Spain*

E-mail: reza.r.zamani@gmail.com; arbiol@icrea.cat

[*]To whom correspondence should be addressed
[†]Institut de Ciència de Materials de Barcelona (ICMAB-CSIC)
[‡]Catalonia Institute for Energy Research (IREC)
[¶]Forschungszentrum Jülich GmbH
[§]Universitat de Barcelona
[∥]Centro S3,CNR–Istituto di Nanoscienze
[⊥]IMEM–CNR
[#]Institució Catalana de Recerca i Estudis Avançats (ICREA)

# Supporting Information

# Contents

## Growth mechanism and synthesis conditions

In order to prove the growth mechanism, in Figure 1 we have added TEM images of the nanocrystals at different growth steps, from the first step that the nanocrystals appear as quasi-spherical $Cu_xSe$ nanoparticles, to tetrahedral, pentaterahedral and branched particles. Moreover, low-magnification TEM micrographs and statistical measurements on the size of the nanoparticles in each step are presented in Figures SI 1 and SI 2. In Figure SI 1 we present low-magnification TEM micrographs showing the time evolution of the nanoparticles. At the very early state of the reaction, quasi-spherical $Cu_xSe$ nanocrystals were formed (Figure SI 1a). During the first minute, a progressive change of morphology and composition was observed. The nanoparticles transformed from spheres to tetrahedrons by the incorporation of Sn and Cd atoms in the crystal structure (Figure SI 1b). At this point, $Cu_xSe$ seeds were not observed in the ensemble of nanoparticles. During the next few minutes of the reaction, the tetrahedral quaternary nanocrystals grew into pentatetrahedral nanoparticles (Figure SI 1c). At this stage of the reaction, one can find some single tetrahedra into the solution, but their content is minimal. Finally, the secondary tetrahedra branch out and the polypods are formed (Figure SI 1d).

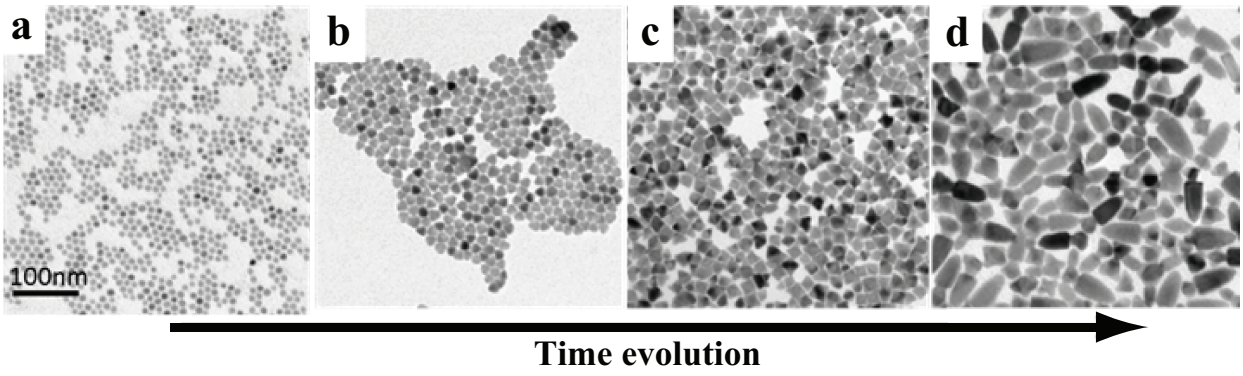


Figure SI 1: TEM images of the nanoparticles obtained at different reaction times at 285 ℃: (a) 10s, (b) 1 min, (c) 5 min, (d) 10 min.

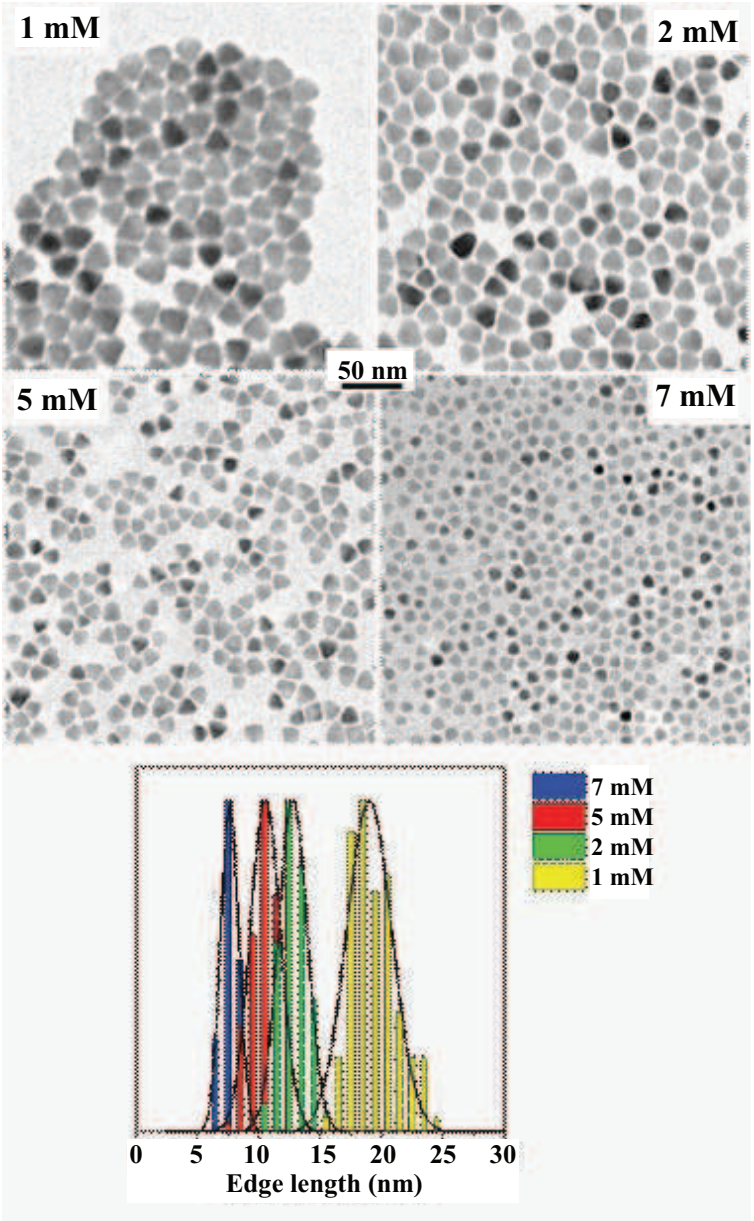


Figure SI 2: TEM images of the tetrahedral nanoparticles obtained at 285 ℃ using different concentration of hexadecylamine: from 1mM to 7 mM.

## EELS compositional maps

EELS compositional maps are shown in Figure SI 3. It is observed that the content of the Cu in the seed and Cd in the branch is relatively higher.

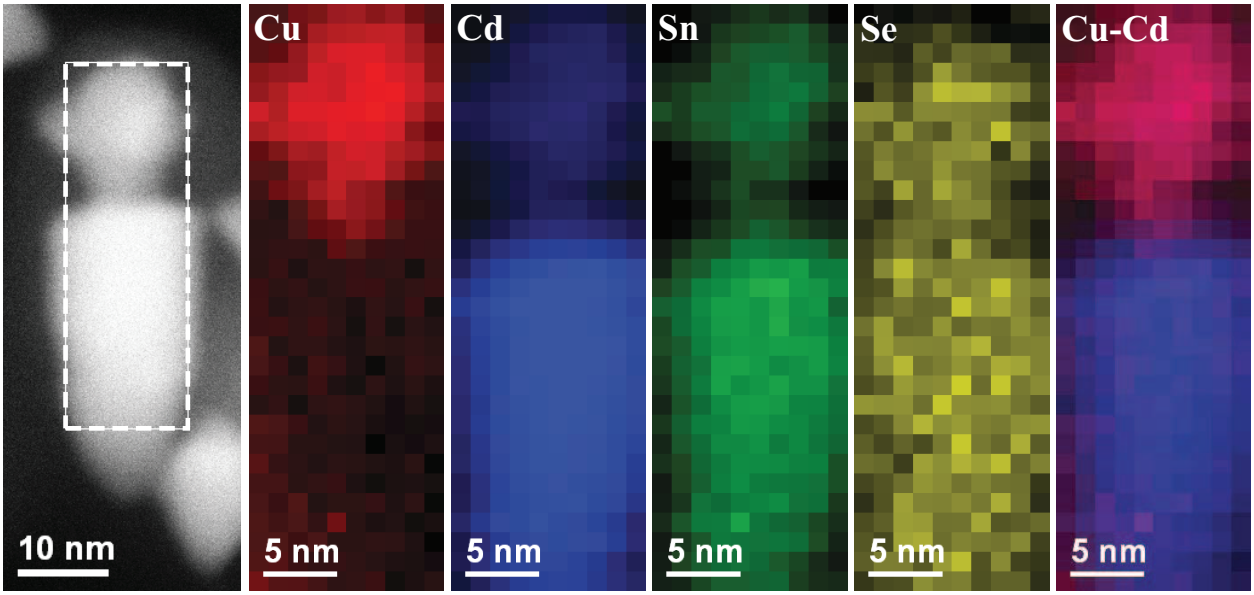


Figure SI 3: EELS elemental map of the indicated rectangle on a CCTSe monopod. The content of Cd is significantly higher in the branches with WZ structure.

## Intensity of cation and anion atomic columns in HAADF images

The intensity of a STEM-HAADF strongly depends on the atomic number Z due to detection of incident electrons that are scattered close to the atomic nuclei. This property makes HAADF-STEM a popular choice for chemically sensitive imaging.[1] For a single atom the intensity is roughly proportional to $Z^2$ because of Rutherford scattering. In a crystalline compound channeling effects occur upon propagation of the electrons through the crystal and the total intensity recorded from a string of aligned atoms is in general not a simple linear sum of individual atom contributions. The depth and orientation dependence of the signal of single dopant tracer atoms elucidates the limitations of the Z-contrast interpretation.[2,3]

However, in the limit of thin samples with a thickness of less than about 10 nm a monotoneous relationship between the average HAADF column intensity and the average Z number of the column is maintained. The following comparison between the average $Z^2$ of anion and cation columns is therefore used as a qualitative criterion for the relation between the HAADF intensity of atomic columns in CCTSe. To analyse polarity in CCTSe in experiment care was taken to record images at sufficiently thin specimen locations.

In anion sites we only have Se ($Z_{Se} = 34$), whereas in cation sites Cu ($Z_{Cu} = 29$), Cd ($Z_{Cd} = 48$), and Sn ($Z_{Sn} = 50$) are positioned. Therefore, regarding the stoichiometry of $Cu_2CdSnSe_4$ the average $Z^2$ of the cations in the zinc-blende-like stannite seeds will be $Z^2_{cat} = 1622$:

$$Z^2_{cat} = \frac{2 \times Z^2_{Cu} + Z^2_{Cd} + Z^2_{Sn}}{4}$$

which is relatively close to the one of anion ($Z^2_{Se} = 1156$). On the other hand, higher content of Cu ($Cu_{2+x}Cd_{1-x}SnSe_4$ as discussed in the paper), further reduces this difference. However, still the polarity is distinguishable from the intensity profiles. As a matter of fact, in the literature, even smaller differences in compounds like GaAs were utilized for polarity determination. In the branch the Cd content is much higher, and consequently, as Cd is much heavier than Se, polarity determination is quite straightforward. With $Cu_2Cd_7SnSe_{10}$ stoichiometry, $Z^2_{cat} = 2031$ which is almost twice of the one of the anion:

$$Z^2_{cat} = \frac{2 \times Z^2_{Cu} + 7 \times Z^2_{Cd} + Z^2_{Sn}}{10}$$

Therefore, in the intensity profiles of Figure 5d, cation-polarity in the wurtzite branch is clearer, *i.e.* the difference of intensity between the cation and the anion is higher. Simulated images are shown in Figure 5c. Moreover, the model and the simulated STEM images of the entire monopod are revealed in Figure SI 4. In this figure, the models (b, c, e, f, and h) and simulated STEM images (d, g, and i) are shown from two viewing directions: [021] (b-d) and [111] (e-i).

## Proper zone axes for dumbbell and ordering visualization

The HAADF micrograph of Figure 6a reveals the ordering of the cations in the seed. Here we explain why [111] zone axis is the only choice for visualization of the cations.

Basically, [201] zone axis which is the best for visualization of the dumbbell units does

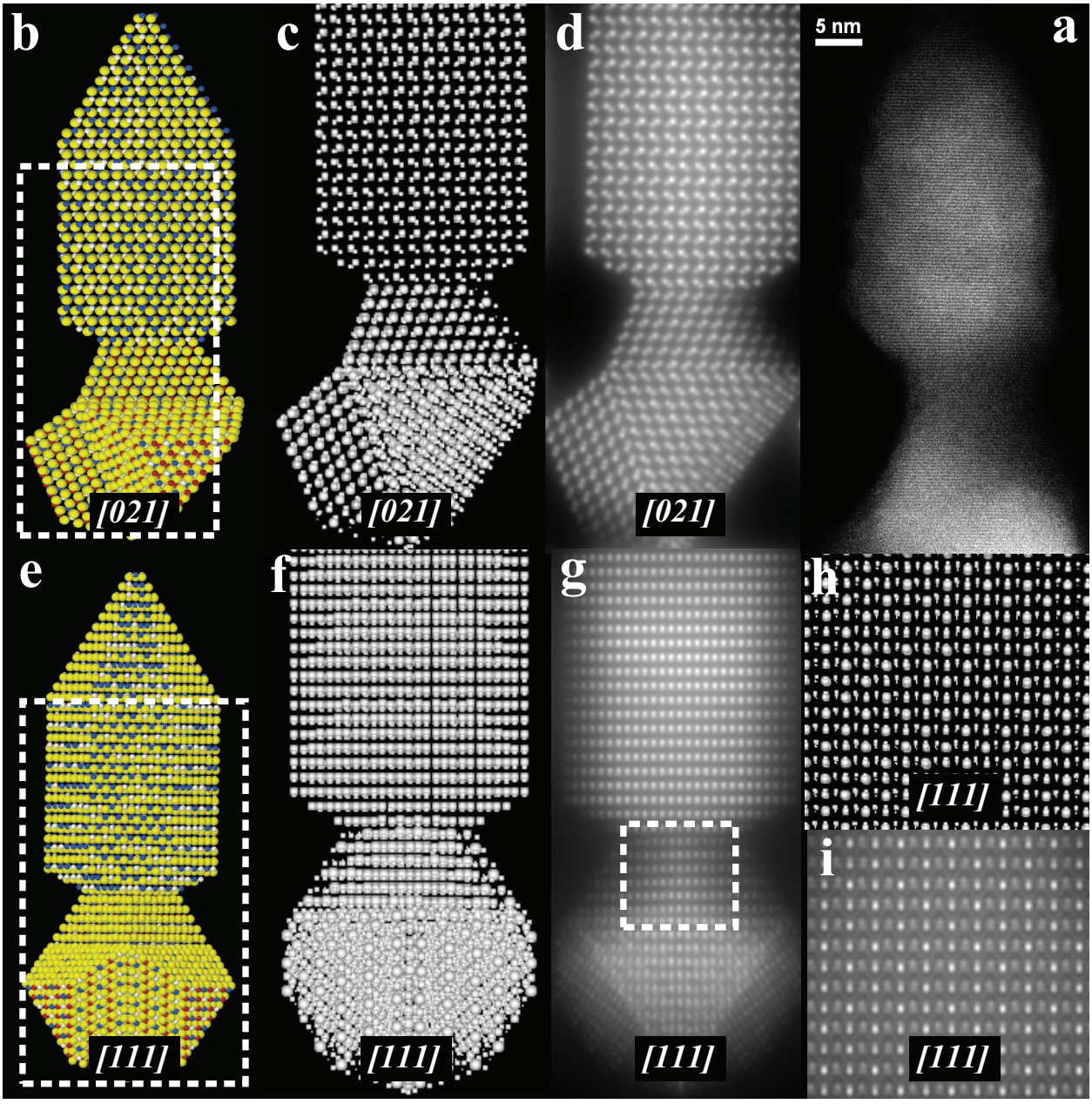


Figure SI 4: STEM image simulation: (a) HAADF-STEM image, (b), (c), (e), (f), (h) atomic models, and (d), (g), (i) STEM simulated images from two viewing directions: (b)-(d) [021], and (e)-(i) [111]

not allow us to see the cation ordering, because in each cation column all Cu, Cd and Sn atoms overlap. To facilitate the comprehension, 3D atomic model of this structure is shown from different angles in Figure 6g and, as a contract, we define the viewing coordination as x: horizontal, y: vertical, and z: viewing axis coming out from the screen. In fact in

the zinc-blende-like structure, three zone axes are proper for dumbbell visualization: [201], [021], and [110]. From [201] and [021] axes, each atomic column related to cation sites in HRTEM/STEM micrographs (in z direction) contains all Cu, Cd and Sn atoms. From [110], nevertheless, Cu columns get separated from the other two elements. Hence, ordering effect should be partially visible. However, Cd and Sn columns are still superposed along the z direction. In contrast, [111] is the only zone axis that allows observing the stannite ordering as none of these elements are superposed with the others. It can be seen in Figure 6g that from this zone axis, in x direction, vertical Cu columns and Cd-Sn columns alternate and further, Cd columns and Sn columns alternate in y direction. Note that from [241] and [421] zone axes which are almost equivalent to [111], ordering effect cannot be seen either. Therefore, [111] zone axis is the only possibility for visualization of cation ordering. The simulated image in Figure 6d and Figure SI 4i.

## Electronic band structure, *ab initio* calculations

To model the experimental stoichiometric wurtzite compound ($Cu_2Cd_7SnSe_{10}$) a $2 \times 2 \times 2$ supercell was created with the atomic relation ($Cu_3Cd_{11}Sn_2Se_{16}$ (to be compared to the stannite supercell explained in Ref.[4] ($Cu_4Cd_2Sn_2Se_8$)).

Four different structures were created: "random-1" and "random-2" have all the atoms randomly distributed, whereas "plane-1" and "plane-2" have all the Cu atoms at the same plane with randomly distribution of the other atoms. We can see that there is not a significant difference between the different distributions.

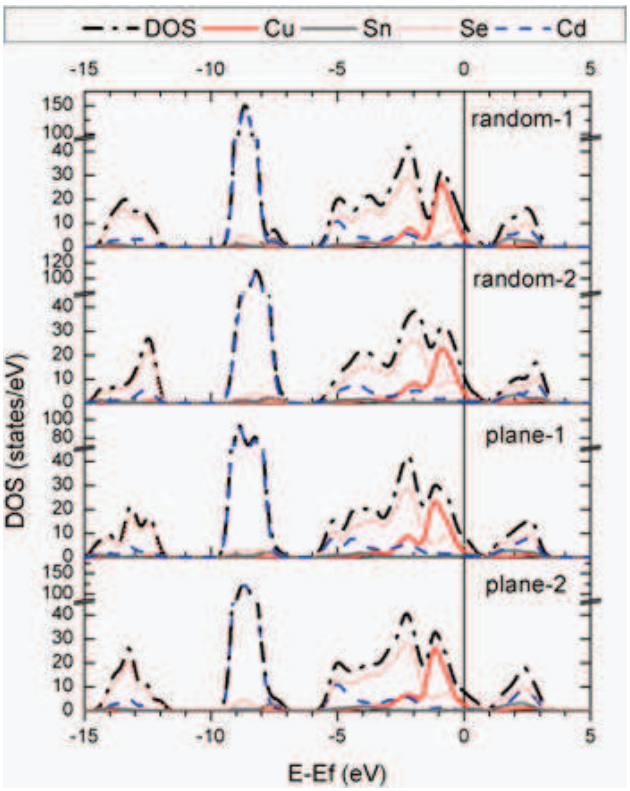


Figure SI 5: Density of states of different randomly distributed wurtzite structures.

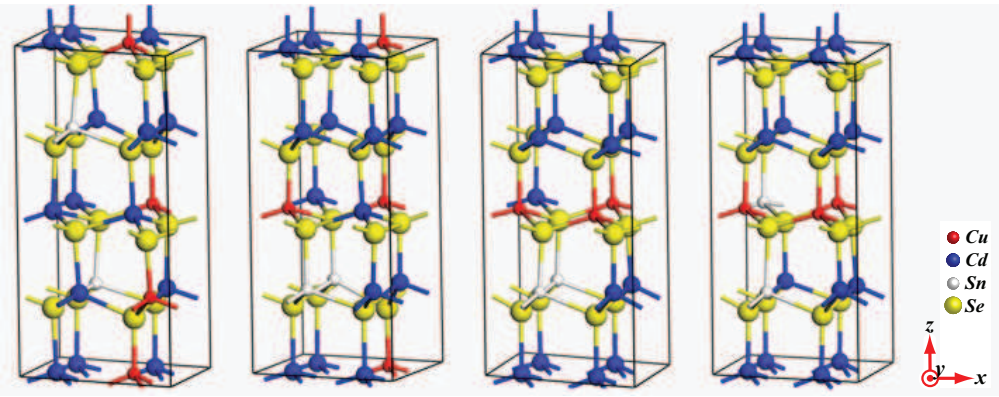


Figure SI 6: Ball and stick configuration of the randomly distributed wurtzite systems. From left to right: random-1, random-2, plane-1, and plane-2.

## References

1. Pennycook, S. J. Z-Contrast Stem for Materials Science. *Ultramicroscopy* **1989**, *30*, 58–69.

2. Voyles, P. M.; Grazul, J. L.; Muller, D. A. Imaging Individual Atoms Inside Crystals with ADF-STEM. *Ultramicroscopy* **2003**, *96*, 251–273, Proceedings of the International

Workshop on Strategies and Advances in Atomic Level Spectroscopy and Analysis.

3. Bar-Sadan, M.; Barthel, J.; Shtrikman, H.; Houben, L. Direct Imaging of Single Au Atoms Within GaAs Nanowires. *Nano Lett.* **2012**, *12*, 2352–2356.

4. Ibáñez, M.; Cadavid, D.; Zamani, R.; García-Castelló, N.; Izquierdo-Roca, V.; Li, W.; Fairbrother, A.; Prades, J. D.; Shavel, A.; Arbiol, J. *et al.* Composition Control and Thermoelectric Properties of Quaternary Chalcogenide Nanocrystals: The Case of Stannite $Cu_2CdSnSe_4$. *Chem. Mater.* **2012**, *24*, 562–570.